

Loss Cone Shielding

Odelia Teboul¹*, Nicholas C. Stone¹, Jeremiah P. Ostriker²

¹*Racah Institute of Physics, The Hebrew University, 91904, Jerusalem, Israel*

²*Department of Astronomy, Columbia University, 550 West 120th St, New York, NY 10027, USA*

Accepted XXX. Received YYY; in original form ZZZ

ABSTRACT

A star wandering close enough to a massive black hole (MBH) can be ripped apart by the tidal forces of the black hole. The advent of wide-field surveys at many wavelengths has quickly increased the number of tidal disruption events (TDEs) observed, and has revealed that i) observed TDE rates are lower than theoretical predictions and ii) E+A galaxies are significantly overrepresented. This overrepresentation further worsens the tension between observed and theoretically predicted TDEs for non-E+A galaxies. Classical loss cone theory focuses on the cumulative effect of many weak scatterings. However, a strong scattering can remove a star from the distribution before it can get tidally disrupted. Most stars undergoing TDEs come from within the radius of influence, the densest environments of the universe. In such environments, close encounters rare elsewhere become non-negligible. We revise the standard loss cone theory to take into account classical two-body interactions as well as strong scattering, collisions, tidal captures, and study under which conditions close encounters can shield the loss cone. We i) analytically derive the impact of strong scattering and other close encounters, ii) compute time-dependent loss cone dynamics including both weak and strong encounters, and iii) derive analytical solutions to the Fokker-Planck equation with strong scattering. We find that i) TDE rates can be reduced to up to an order of magnitude and ii) strong shielding preferentially reduces deeply plunging stars. We also show that stellar overdensities, one possible explanation for the E+A preference, can fail to increase TDE rates when taking into account strong scattering.

Key words: transients: tidal disruption events – galaxies: kinematics and dynamics – stars: kinematics and dynamics – methods: analytical - methods: numerical

1 INTRODUCTION

A star wandering too close to a massive black hole (MBH) can be ripped apart by the MBH’s tidal forces. Roughly half of the gaseous debris from the disrupted star falls back onto the MBH, eventually circularizing into an accretion disk and powering a luminous flare (Rees 1988; Evans & Kochanek 1989).

Tidal disruption events (TDEs) have been theoretically predicted since the 1970s (e.g., Hills 1975) but were not observed until the advent of all-sky surveys (beginning with the ROSAT X-ray all-sky survey; Bade et al. 1996; Komossa & Bade 1999). The sample of observed TDEs has rapidly grown in the last decades and now spans all wavelengths, from the radio to gamma-rays. The last decade has seen a high rate of TDE discovery in wide-field optical surveys such as SDSS (van Velzen et al. 2011), Pan-STARRS (Gezari et al. 2012; Chornock et al. 2014; Nicholl et al. 2019), PTF (Arcavi et al. 2014), iPTF (Blagorodnova et al. 2019; Hung et al. 2017), ASASSN (Holoi et al. 2016; Hinkle et al. 2021), and ZTF (van Velzen et al. 2019; Hammerstein et al. 2022). X-

ray surveys are also returning to prominence as a driver of TDE discovery; at present, the SRG/eROSITA all-sky survey (Sazonov et al. 2021) seems to be finding ~ 20 TDEs per year, comparable to the optical TDE discovery rate of ZTF. As time domain capabilities continue to expand, the observed sample of TDEs is expected to grow by orders of magnitude, with hundreds to thousands of new TDEs expected to be found in optical wavelengths by the LSST/Vera Rubin Observatory (Ivezic et al. 2019; Bricman & Gomboc 2020), and in the near-ultraviolet by ULTRASAT (Ben-Ami et al. 2022).

The opening of this new era for TDEs has allowed observers to empirically constrain the per-galaxy TDE rate to a range $\dot{N}_{\text{TDE}} \sim 10^{-5} - 10^{-4} \text{ yr}^{-1} \text{ gal}^{-1}$ (Holoi et al. 2016; van Velzen 2018), and revealed a surprising over-representation of these events in post-starburst (e.g. “E+A”) galaxies (Arcavi et al. 2014; French et al. 2016, 2017; Law-Smith et al. 2017; Graur et al. 2018; French et al. 2020; Hammerstein et al. 2021). The latest estimations suggest that E + A galaxies are overrepresented by a factor of ≈ 22 (Hammerstein et al. 2021). This further reduces the observationally inferred TDE rate in non-E+A galaxies, which is already in tension with theoretical (but empirically calibrated) rate estimates of $\dot{N} \sim$

* E-mail: odelia.teboul1@mail.huji.ac.il

$10^{-4} - 10^{-3}$ yr $^{-1}$ gal $^{-1}$ (Wang & Merritt 2004; Stone & Metzger 2016).

TDE rates are traditionally estimated from classical loss cone theory, which focuses on the cumulative effect of many weak scatterings. These scatterings are modeled as local and uncorrelated, and lead to effective diffusion coefficients describing the drift and diffusion of stellar populations through phase space (see Merritt 2013; Stone et al. 2020, for reviews). Strong, or small impact parameter scatterings are generally neglected, as they are largely outnumbered by weak scatterings.

However, strong scatterings can have a qualitatively different effect than weak ones on stellar populations. In particular, *a strong scattering can eject a star from the distribution* before it gets tidally disrupted. Most stars undergoing TDEs come from within the radius of influence, *the densest environments in the Universe*. Such an environment can facilitate ejection in strong scatterings, but it also increases the rate of close encounters that are rare elsewhere. Such close encounters can be divided into star-star interactions, including collisions and tidal captures, and star-stellar mass black hole (sBH) interactions, such as μ -TDEs and tidal captures. In this paper we will revise the standard loss cone theory to take into account not simply weak two-body scatterings, but also destructive processes such as strong scattering ejections, collisions, and tidal captures, with the ultimate goal of determining under which conditions close encounters can *shield the loss cone*.

Close encounters are highly dependent on both the stellar and sBH slopes. An important prediction of stellar dynamics is the redistribution of arbitrary initial distributions of stars around MBHs over time into quasi-stationary states (QSSs). In the presence of one population of stars, a Bahcall-Wolf density cusp with stellar density $\rho \propto r^{-\gamma}$, will develop, with $\gamma = 7/4$ (Bahcall & Wolf 1976a). If the system is composed of both stars and heavier objects, the heavier objects are expected to segregate towards the centre of the galactic nucleus and settle on a steeper cusp $\gamma = 7/4 - 2$ while the light objects will have a weaker cusp $\gamma \approx 1.3 - 1.5$ (Bahcall & Wolf 1977; Preto & Amaro-Seoane 2010a; Amaro-Seoane & Preto 2011; Broggi et al. 2022). In the strong segregation limit, when the heavier objects are relatively rare, the heavy objects have been predicted to settle to even steeper power-law slopes of $\gamma = 2 - 11/4$ (Alexander & Hopman 2009).

We introduce the different kinds of close encounters that are relevant for our problem in §2, and derive their analytical rates in §2.2. In §3, we solve the Fokker-Planck equation in angular momentum space in the presence of close encounters. In 3.3 we present our analytical time-dependent solutions of the Fokker-Planck equation with strong scattering. In §4 we compute the impact of close encounters on TDE rates and discuss our findings for the E+A preference. In §5, we discuss the implications of our work and briefly summarize it.

2 CLOSE ENCOUNTERS

In a spherical galactic nucleus one can characterize the population of stars with an orbit-averaged distribution function $f(E, L)$, where E is the orbital energy and L the orbital angular momentum of stars. A variety of processes can remove stars from the distribution f . Most notably, a star of mass M_*

and radius R_* will be destroyed by the central MBH (of mass M) if it completes an orbit with galactocentric pericenter R_p less than the tidal radius,

$$R_t = R_* \left(\frac{M}{M_*} \right)^{1/3}. \quad (1)$$

A finite R_t (i.e. the presence of a central MBH) carves a conical gap in velocity space (at fixed radius), or equivalently places a non-zero lower limit on the angular momentum that particle orbits may have (Frank & Rees 1976; Lightman & Shapiro 1977; Cohn & Kulsrud 1978). Particles with less angular momentum suffer destructive interactions at pericenter.

However, before the typical star can get to an orbit with $R_p \sim R_t$, its pericenter must endure a long and potentially dangerous random walk through regions of high stellar and sBH density. During this random walk, sufficiently close encounters with the stellar/sBH population can eliminate our test star through a variety of different processes. Here we overview the relevant ones, roughly in order of increasing cross-section:

(i) Direct physical collisions: star-star (or star-sBH) collisions with a pairwise pericenter $p < R_*$ will often destroy the test star. At large distances r from the MBH, where the velocity dispersion $\sigma \ll V_* = \sqrt{2GM_*/R_*}$, the stellar surface escape speed, collisions with other stars can be coagulative rather than destructive¹.

(ii) μ -TDEs: slightly more distant encounters with a sBH ($p < r_t$, where r_t is the same as R_t from Eq. 1 but with the sBH mass m_{bh} substituted into Eq. 1 for M), can destroy the test star through the action of the sBH's tides, in a scaled down version of a standard TDE. The observational signatures of these “ μ -TDEs” are poorly understood (Perets et al. 2016). However, the different dynamics and greatly reduced Eddington limit of an sBH (compared to an MBH) means that the resulting transient is unlikely to be mistaken for a standard TDE, and a star experiencing this fate can be safely removed from the distribution function.

(iii) Tidal captures: at slightly larger pericenter distances than the μ -TDE radius, tides can excite mechanical oscillation modes in the test star. If this process converts enough orbital energy into mechanical energy, then an unbound parabolic/hyperbolic two-body orbit will capture into a bound binary (Fabian et al. 1975; Press & Teukolsky 1977; Lee & Ostriker 1986). A tidal capture can only occur when the relative kinetic energy between the two objects is less than the binding energy of the test star. The long-term evolution of a tidal capture system is not entirely clear (Generozov et al. 2018). Some recent hydrodynamical simulations indicate that the captured star will be destroyed in a brief sequence of runaway partial (micro)-TDEs (Kremer et al. 2022), but even if this is not the case, a star that has become tightly bound to a sBH is unlikely to ever experience a TDE. If a tight binary's center-of-mass angular momentum starts falling to levels approaching the loss cone, then direct merger (i.e. μ -TDE) becomes the most probable outcome (Bradnick et al. 2017), followed by tidal separation via the Hills mechanism. Star-star tidal captures are also possible, but again the most likely final result (if the binary is excited towards small p

¹ As we are focused on relatively small spatial scales, we neglect this possibility in this paper.

values) is a merger, which would effectively remove one star from the distribution function.

(iv) Ejections: a strong (large-angle) scattering between the test star and another stellar-mass object can accelerate it above the local escape speed, v_{esc} . When this happens, the star is removed from the system (Lin & Tremaine 1980) and can, under certain conditions, become a hypervelocity star (Yu & Tremaine 2003; O’Leary & Loeb 2008). We note that some recent efforts have examined the role of strong scatterings in affecting the final parameters of loss cone orbits (Weissbein & Sari 2017, 2021), but this is distinct from ejection and loss cone shielding.

We will now calculate the different rates of the processes that can remove stars from the distribution. We will begin with an order of magnitude estimate which allow us to find the correct scaling relationship. We will then present our analytical derivations for each kind of close encounters.

2.1 Approximate Description

The rates of processes (i-iv) are governed by basically the same underlying physics, and can be calculated in the usual “ $n - \Sigma - v$ ” way as

$$\dot{N} = n\pi p_c^2 \left(1 + \frac{2G(M_\star + m_2)}{p_c v^2} \right) v_\infty, \quad (2)$$

where \dot{N} is the per-target rate of close encounters, p_c is the critical pericenter for the close encounter (e.g. direct collision, μ -TDE, or tidal capture) to occur, v_∞ is the relative velocity at infinity, M_\star is the mass of the target star, $M_{\bullet 2}$ is the mass of the secondary (another star for star-star encounters or a sBH for TCs/ μ -TDEs), and n is the number density of secondaries.

Far from the central MBH, the rates of these close encounters will be set by gravitational focusing, but close to the MBH, encounter rates will be determined by straight-line flyby trajectories. We will now approximate the rates of close encounters in these two regimes by making the simplified assumption that all stars have the same mass M_\star and are distributed in space with a power-law $n_\star(r) \propto r^{-\gamma_\star}$, and likewise that all sBHs have a common mass m_{bh} and a power-law density profile $n_{\text{bh}}(r) \propto r^{-\gamma_{\text{bh}}}$. We further approximate the situation by assuming that all relative velocities are equal to the stellar velocity dispersion,

$$\sigma_\star = \sqrt{\frac{GM_\star}{r(1 + \gamma_\star)}}, \quad (3)$$

sparing us the need to integrate over a relative velocity distribution. Under these simplifying assumptions, the (per-target) rates of star-star collisions, star-sBH μ -TDEs, and star-sBH tidal captures scale, respectively, as

$$\dot{N}_{\text{coll}} \propto \begin{cases} R_\star^2 r^{-\gamma_\star - 1/2}, & r < r_{\text{coll}}^{\text{tr}} \\ R_\star M_\star r^{-\gamma_\star + 1/2}, & r > r_{\text{coll}}^{\text{tr}} \end{cases} \quad (4)$$

$$\dot{N}_{\mu\text{TDE}} \propto \begin{cases} R_\star^2 \alpha^{-2/3} r^{-\gamma_{\text{bh}} - 1/2}, & r < r_{\mu\text{TDE}}^{\text{tr}} \\ R_\star m_{\text{bh}}(1 + \alpha) \alpha^{-1/3} r^{-\gamma_{\text{bh}} + 1/2}, & r > r_{\mu\text{TDE}}^{\text{tr}} \end{cases} \quad (5)$$

$$\dot{N}_{\text{TC}} \propto \begin{cases} \lambda^2 R_\star^2 \alpha^{-2/3} r^{-\gamma_{\text{bh}} - 1/2}, & r < r_{\text{TC}}^{\text{tr}} \\ \lambda R_\star m_{\text{bh}}(1 + \alpha) \alpha^{-1/3} r^{-\gamma_{\text{bh}} + 1/2}, & r > r_{\text{TC}}^{\text{tr}}. \end{cases} \quad (6)$$

Here the transition radii between the focused and unfocused interaction regimes are

$$r_{\text{coll}}^{\text{tr}} = \frac{R_\star}{4(1 + \gamma_\star)} \frac{M_\bullet}{M_\star} \approx 2 \times 10^{-3} \text{ pc } M_6 r_\star m_\star^{-1} \quad (7)$$

$$r_{\mu\text{TDE}}^{\text{tr}} = \frac{R_\star}{2(1 + \gamma_{\text{bh}})} \frac{\alpha^{2/3}}{1 + \alpha} \frac{M_\bullet}{M_\star} \approx 8 \times 10^{-4} \text{ pc } M_6 r_\star m_\star^{-1} \quad (8)$$

$$r_{\text{TC}}^{\text{tr}} = \frac{\lambda R_\star}{2(1 + \gamma_{\text{bh}})} \frac{\alpha^{2/3}}{1 + \alpha} \frac{M_\bullet}{M_\star} \approx 2 \times 10^{-3} \text{ pc } M_6 r_\star m_\star^{-1}, \quad (9)$$

and we have further defined $\alpha = M_\star/m_{\text{bh}}$ as the sBH-star mass ratio, and $\lambda \approx 2$ as the rough enhancement to the μ -TDE cross-section for tidal captures². In the approximate equalities above, we have taken $\gamma_\star = \gamma_{\text{bh}} = 7/4$, $\lambda = 2$, and $\alpha = 0.1$ for concreteness, and used the shorthand variables $M_6 = M/(10^6 M_\odot)$, $m_\star = M_\star/M_\odot$, and $r_\star = R_\star/R_\odot$.

It is important to note that tidal capture becomes impossible when the relative kinetic energy of the target and secondary becomes larger than the maximum amount of mechanical energy that can be injected into the target star’s normal modes in a single pericenter passage. Crudely approximating this condition as $M_\star m_{\text{bh}}(M_\star + m_{\text{bh}})^{-1} \sigma^2/2 > u_\star GM_\star^2/R_\star$, where $u_\star < 1$ is a fudge factor representing the fraction of the star’s binding energy that can be absorbed by mechanical oscillations, we find that tidal capture deactivates at radii below

$$r_{\text{TC}} = \frac{R_\star}{2u_\star(1 + \gamma_\star)} \frac{1}{1 + \alpha} \frac{M}{M_\star}. \quad (10)$$

Because $r_{\text{TC}} \sim r_{\text{TC}}^{\text{tr}} \alpha^{-2/3} u_\star^{-1}$, and most likely $u_\star \sim \mathcal{O}(0.1)$, r_{TC} is generally greater than $r_{\text{TC}}^{\text{tr}}$ and tidal captures are always gravitationally focused.

We also want to understand the basic scaling laws describing rates of stellar ejection through strong scatterings. We approximate the specific impulse delivered to the target star in a strong scattering as $\Delta v \sim (Gm_2/p^2)(p/v_p)$, with v_p the velocity at pericenter. Angular momentum conservation lets us rewrite this in terms of the velocity (v_∞) and impact parameter (b) at infinity: $\Delta v \sim Gm_2/(bv_\infty)$. Thus the critical impact parameter that allows strong scatterings to eject stars will be $b_{\text{ej}} = Gm_2/(v\Delta v_{\text{ej}})$, where Δv_{ej} is the critical specific impulse to eject a star. While it is tempting to equate $\Delta v_{\text{ej}} = v_{\text{esc}}(r) = \sqrt{2GM/r}$, we must remember that for stars on loss cone orbits, $1 - e \ll 1$ and most of the orbit is spent traveling at speeds $v(r) \approx v_{\text{esc}}(r)$. Therefore we approximate $\delta v_{\text{ej}} \approx v_{\text{esc}}(r) - v(r)$, or

$$\Delta v_{\text{ej}} \approx \frac{1}{2\sqrt{2}} \sqrt{\frac{GMr}{a^2}} \quad (11)$$

for a star on a highly eccentric orbit with $r \ll a$. We now see that the critical impact parameter for ejection is $b_{\text{ej}} \sim 2\sqrt{2}am_2/M$. The local ejection rate from scatterers with number density n will thus be $\dot{N}_{\text{ej}} = n\pi b_{\text{ej}}^2 v_\infty$, so that

$$\dot{N}_{\text{ej}} \propto a^2 m_2^2 r^{-\gamma - 1/2}. \quad (12)$$

Here we have left m_2 and γ general, as they may represent either star-star or star-sBH strong scatterings. In contrast to

² In reality, $\lambda \sim \mathcal{O}(1)$ depends weakly on the local properties of the background cluster (Lee & Ostriker 1986).

Eqs. 4–6, there is no leading-order distinction between gravitationally focused or unfocused regimes for strong scatterings. Furthermore, there is no leading-order dependence on the mass m_* of the test star experiencing the scattering (although note that this equation implicitly assumes $m_* \lesssim m_2$).

While Eqs. 4–6 and 12 give local encounter rates $\dot{N}(r)$, we also want to compute their orbit-averaged versions, $\langle \dot{N} \rangle$. Because of our ultimate interest in the loss cone, we consider highly eccentric orbits with pericenter $p \ll a$, the stellar semimajor axis. At the order of magnitude level, we can approximate the orbit-averaged rate of some process at a given radius as $\langle \dot{N}(r) \rangle \sim \dot{N}(r) \times (r/a)^{3/2}$, and determine whether the rates are pericenter- or apocenter-dominated to get $\langle \dot{N} \rangle$.

For ejection in strong scatterings,

$$\langle \dot{N}_{\text{ej}} \rangle \propto a^{1/2} p^{-\gamma+1} m_2^2, \quad (13)$$

so ejection rates will be pericenter-dominated as long as $\gamma > 1$, which we will assume for the remainder of this paper (as none of the close encounter rates we consider are interestingly high for shallow cusps). For other types of close encounters, encounter rates will likewise be pericenter-dominated at small radii $r < r^{\text{tr}}$ so long as $\gamma > 1$, but the situation at large radii $r > r^{\text{tr}}$ is more complicated. From Eqs. 4–6, we see that close encounter rates will always be pericenter-dominated when $\gamma > 2$, but when $1 < \gamma < 2$, the situation depends on whether $p > p^{\text{tr}}$, a transitional pericenter³. More specifically, we find that when $1 < \gamma < 2$, close encounter rates scale as

$$\langle \dot{N}_{\text{ce}} \rangle \propto \begin{cases} p^{-\gamma+1} a^{-3/2} R_{\text{ce}}^2, & p < p^{\text{tr}} \text{ or } a < r^{\text{tr}} \\ a^{-\gamma+1/2} R_{\text{ce}}, & p > p^{\text{tr}} \text{ or } p > r^{\text{tr}} \end{cases} \quad (14)$$

Here we have approximated the transitional pericenter as

$$p^{\text{tr}} \sim a \left(\frac{R_{\text{ce}} M}{a(M_* + m_2)} \right)^{1/(\gamma-1)}. \quad (15)$$

Note that it is possible for $p^{\text{tr}} > a$; in this situation, rates are always pericenter-dominated, so even though p^{tr} no longer has a physical meaning, the inequality conditions in Eq. 14 are still accurate.

Alternatively, when $\gamma > 2$,

$$\langle \dot{N}_{\text{ce}} \rangle \propto \begin{cases} p^{-\gamma+1} a^{-3/2} R_{\text{ce}}^2, & p < r^{\text{tr}} \\ p^{-\gamma+2} a^{-3/2} R_{\text{ce}}, & a > r^{\text{tr}}. \end{cases} \quad (16)$$

Because of the many permutations of possibilities, we have not disaggregated collision, μ -TDE, and tidal capture rates in the above formulae, instead referring to a “close encounter radius” R_{ce} which will be equal to R_* , r_t , or r_{TC} for these three processes, respectively. Likewise, we have denoted a general transition radius r^{tr} differentiating between focused and unfocused local encounter rates; the appropriate transitional radius should be chosen from among Eqs. 7–9.

With these scaling relations in hand to provide physical intuition, we now proceed to more rigorously derive ejection and close encounter rates.

2.2 Strong Scatterings

In this section, we present our analytical derivations of orbit-averaged rates for strong scattering. We employ a stellar dis-

³ If $\gamma = 2$, then rates are pericenter-dominated for $p < r^{\text{tr}}$, but each decade in radius contributes equivalently when $p > r^{\text{tr}}$.

tribution function calculated under the assumptions that (i) the stellar density profile $\rho(r) = \rho_{\text{infl}}(r/r_{\text{infl}})^{-\gamma_*}$, and (ii) the potential $\psi = GM_*/r$ is everywhere Keplerian⁴. Under the assumption of isotropy, we apply an Eddington integral to ρ to obtain

$$f_*(\epsilon) = 8^{-1/2} \pi^{-3/2} \frac{\Gamma(\gamma_* + 1)}{\Gamma(\gamma_* - 1/2)} \frac{\rho_{\text{infl}}}{\langle m_* \rangle} \left(\frac{GM_*}{r_{\text{infl}}} \right)^{-\gamma_*} \epsilon^{\gamma_* - 3/2} \quad (17)$$

where the (positive-definite) specific orbital energy is, for a given star at radius r and velocity v , $\epsilon = \psi(r) - v^2/2$; $\langle m_* \rangle$ is the average mass in the stellar population; and r_{infl} is the radius that encloses a mass in stars equal to the MBH mass.

2.2.1 Equal mass scatterer

We first consider strong scattering from an equal mass scatterer, e.g., from other stars. We will assume that all stars have the same mass m_* and that the distribution of velocities is isotropic at every point. Let us consider a test star whose velocity is \mathbf{V} . The probability for such a star to have an encounter during a time dt that will increase its velocity to $\mathbf{V} + \delta\mathbf{v}$ is (Hénon 1960a):

$$P = \frac{8\pi G^2 m_*^2 dt}{\delta v^5} d\delta v_x d\delta v_y d\delta v_z \int_{v_0}^{\infty} f_*(v) v dv \quad (18)$$

where $f_*(v)$ is the distribution function of stars and v_0 is given by:

$$v_0 = \frac{1}{\delta v} |\mathbf{V} \cdot \delta\mathbf{v} + \delta v^2|. \quad (19)$$

Let θ be the angle between \mathbf{V} and $\delta\mathbf{v}$, with v_{esc} the escape velocity at this point. The star will be ejected if:

$$V^2 + \delta v^2 + 2V\delta v \cos \theta \geq v_{\text{esc}}^2. \quad (20)$$

Replacing cartesian coordinates by spherical coordinates, the local ejection rate, i.e. the probability for one star to be ejected during a time dt , is given by (Hénon 1960b):

$$\dot{N}_{\text{ej}} = \frac{32\pi^2 G^2 m_*^2}{3V(v_{\text{esc}}^2 - V^2)^2} \int_{\sqrt{v_{\text{esc}}^2 - V^2}}^{v_{\text{esc}}} (v^2 + V^2 - v_{\text{esc}}^2)^{3/2} f_*(v) v dv. \quad (21)$$

Assuming Keplerian motion (i.e. Eq. 17) and an escape velocity $v_{\text{esc}} = \sqrt{2GM/r}$, the local ejection rate becomes:

$$\dot{N}_{\text{ej}} = \frac{2^{2-\gamma_*} \pi \rho_{\text{infl}} a^2 m_* V^{1+2\gamma_*}}{(1 + \gamma_*) M^2} \left(\frac{GM}{r_{\text{infl}}} \right)^{-\gamma_*} \quad (22)$$

with V the local Keplerian velocity of the test star and a its semimajor axis. As the relaxation time is much longer than an orbital period, the local ejection rate per star can then be orbit-averaged as:

$$\langle \dot{N}_{\text{ej}} \rangle = \frac{2^{2-\gamma_*} \rho_{\text{infl}} m_* G^{1/2} a^{3/2-\gamma_*} r_{\text{infl}}^{\gamma_*}}{(\gamma_* + 1) M^{3/2} (1 - e^2)^{\gamma_* - 1}} \times \int_0^\pi \frac{(1 + e^2 + 2e \cos \nu)^{1/2+\gamma_*}}{(1 + e \cos \nu)^2} d\nu \quad (23)$$

⁴ Throughout the remainder of this paper, we adopt the usual stellar dynamics convention of positive-definite potentials and positive-definite energies for bound orbits.

with ν the true anomaly, and e the eccentricity of the star.

The orbit-averaged ejection rate does not have a general closed form. However, for relevant values of γ_* which are integers or half-integers, an analytical solution exists. Analytic solutions for some interesting values of γ_* are presented in Appendix A (along with some more general notes on orbit-averaging).

2.2.2 Unequal mass scatterer

Let us now consider strong scattering from an unequal mass scatterer, i.e. stellar mass black holes with $\alpha = m_*/m_{\text{bh}}$. The probability for a star with velocity \mathbf{V} to have an encounter during a time dt that will increase its velocity to $\mathbf{V} + \delta\mathbf{v}$ becomes:

$$P = \frac{8\pi G^2 m_{\text{bh}}^2 dt}{\delta v^5} d\delta v_x d\delta v_y d\delta v_z \int_{v_0}^{\infty} f_{\text{bh}}(v) v dv, \quad (24)$$

where $f_{\text{bh}}(v)$ is the distribution function of stellar mass black holes (also assumed to reflect a power-law density profile, with $\rho_{\text{bh}} \propto r^{-\gamma_{\text{bh}}}$), and v_0 is given by:

$$v_0 = \frac{1}{\delta v} |\mathbf{V} \cdot \delta\mathbf{v} + \frac{m_* + m_{\text{bh}}}{2m_{\text{bh}}} \delta v^2| \quad (25)$$

The condition for the star to escape remains unchanged. Therefore, after some algebraic manipulations, the local ejection rate becomes :

$$\dot{N}_{\text{ej,u}} = 16\pi^2 G^2 m_{\text{bh}}^2 \left(\int_{v_1}^{v_2} I_A f_{\text{bh}}(v) v dv + \int_{v_2}^{v_3} I_B f_{\text{bh}}(v) v dv + \int_{v_3}^{v_{\text{esc}}} I_C f_{\text{bh}}(v) v dv \right) \quad (26)$$

where

$$\begin{aligned} I_A &= \frac{2 [v^2 - \alpha (v_{\text{esc}}^2 - V^2)]^{3/2}}{3V (v_{\text{esc}}^2 - V^2)^2} \\ I_B &= \frac{2 [v^2 - \alpha (v_{\text{esc}}^2 - V^2)]^{3/2} + v [2v^2 - 3\alpha (v_{\text{esc}}^2 - V^2)]}{6V (v_{\text{esc}}^2 - V^2)^2} \\ &\quad - \frac{(2v_{\text{esc}} + V)}{6V (v_{\text{esc}} + V)^2} + \frac{(1 + \alpha)^2}{8V (V + v)} \\ I_C &= \frac{3v_{\text{esc}}^2 - V^2}{3(v_{\text{esc}}^2 - V^2)^2} + \frac{(1 + \alpha)^2}{4(V^2 - v^2)} \end{aligned} \quad (27)$$

and the limits of integral are given by:

$$\begin{aligned} v_1 &= \sqrt{\alpha(v_{\text{esc}}^2 - V^2)} \\ v_2 &= \frac{1}{2} [(1 + \alpha)v_{\text{esc}} - (1 - \alpha)V] \\ v_3 &= \frac{1}{2} [(1 + \alpha)v_{\text{esc}} + (1 + \alpha)V] \end{aligned} \quad (28)$$

The local ejection rate per star can then be orbit averaged as in Eq. A2. This orbit-averaged ejection rate does not have a general closed form, although the local ejection rate (Eq. 26) can be written in closed form for special values of γ_{bh} .

2.3 Star-star encounters: physical collisions and tidal captures

Tidal captures and physical collisions between stars, although rare in most astrophysical environments, are non-negligible in the extreme densities of galactic nuclei. Assuming that all stars have the same mass m_* , and that the test star has a velocity \mathbf{V} , the local collision rate is given by

$$\dot{N}_{\text{coll}} = \int d^3\mathbf{v} f(\mathbf{v}) \pi b^2 |\mathbf{V} - \mathbf{v}| \quad (29)$$

with the gravitationally focused impact parameter $b^2 = r_{\text{coll}}^2 + 4Gm r_{\text{coll}}/V_0^2$ and $V_0 = |\mathbf{V} - \mathbf{v}|$. To take into account both collisions and tidal captures from stars we can rewrite the formula as :

$$\dot{N}_{*,*} = 2\pi^2 \int_0^{v_{\text{esc}}} \int_0^{\sqrt{v_{\text{esc}}^2 - v_{\parallel}^2}} \sqrt{(V - v_{\parallel})^2 + v_{\perp}^2} b_{\text{max}}^2 f_{\text{bh}}(v) v_{\perp} dv_{\perp} dv_{\parallel} \quad (30)$$

with $b_{\text{max}}^2 = r_{\text{max}}^2 + 4Gm r_{\text{max}}/V_0^2$, where $r_{\text{max}} = \max[r_{\text{coll}}, r_{\text{capt}}(V_0, m_*)]$ and $r_{\text{capt}} = 2R_{*,*} \approx 2R_*$ is the approximate tidal capture radius we employ for a high- σ environment (Stone et al. 2017). This formula is only an approximation to a more rigorous calculation of the tidal capture radius, (see e.g. Lee & Ostriker 1986), but it will generally be correct to within a few 10s of percent in a high- σ galactic nucleus (Generozov et al. 2018).

Note that tidal capture cannot occur if the relative velocity $V_0 \gtrsim \eta v_*$, where $\eta < 1$ is a dimensionless number of uncertain magnitude. When $V_0 \ll v_*$, tidal capture can proceed cleanly through the linear excitation of normal modes in the star. However, when $V_0 \sim v_*$, the oscillation modes reach nonlinear amplitudes and may begin to dissipate their energy rapidly through nonlinear mode-mode couplings or by steepening into shocks. Rapid dissipation of the mode mechanical energy can inflate the star and result in its destruction via a sequence of partial μ -TDEs (Kremer et al. 2022). The fudge factor η encodes the boundary between successful and unsuccessful captures; for simplicity, in the remainder of this paper we will take $\eta = 0.1$. Regardless of the true value of η , it is clear that at small galactocentric radii, stars are tidally disrupted rather than captured.

The orbit-averaged star-star collision/tidal capture rate $\langle \dot{N}_{*,*} \rangle$ can be computed as per standard orbit-averaging procedures (Eq. A2).

2.4 Star-sBH encounters: μ -TDEs and tidal captures

A star wandering too close to a stellar mass black hole can be tidally captured or tidally disrupted. The characteristic tidal radius is $r_t = r_*(m_{\text{bh}}/m_*)^{1/3}$, while the maximum initial pericentre distance resulting in tidal capture, r_{capt} , is approximated as before by $r_{\text{capt}} = 2r_t$, with the same caveat that large V_0 are treated as μ -TDEs rather than tidal captures.

Considering a test star with velocity \mathbf{V} , its probability to be tidally captured or disrupted by one of the stellar mass black

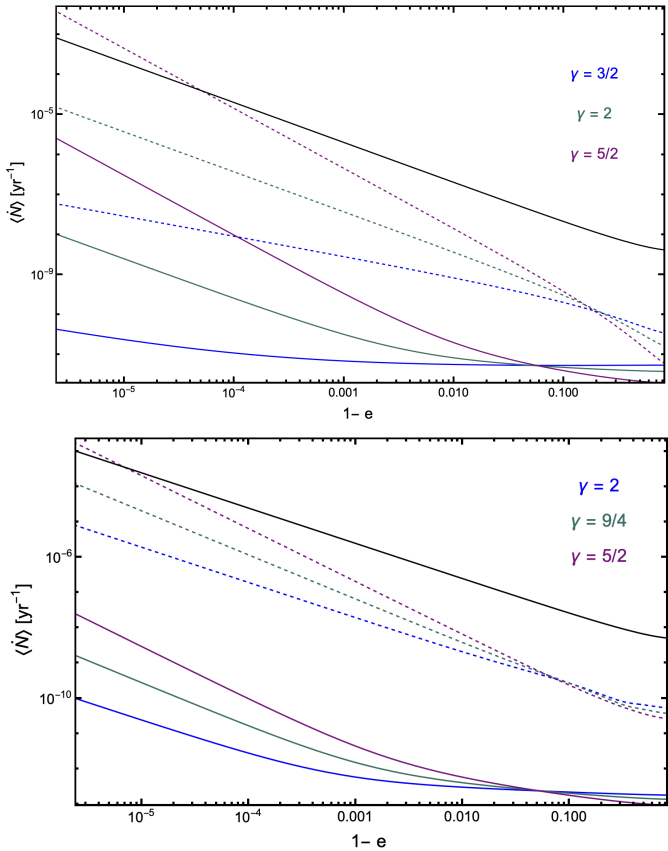


Figure 1. *Top:* Average rates of close encounters between stars, as a function of the dimensionless test star pericenter $1 - e$. The test star has semimajor axis $a = r_{\text{infl}}$ and results are shown for different stellar slopes (color-coded). Dashed lines show strong scattering ejection rates; full lines show tidal captures and stellar collisions. *Bottom:* same as above, but now for unequal-mass encounters between stars and black holes of mass $m_{\text{bh}} = 30M_{\odot}$. In both figures, the inverse angular momentum relaxation time is plotted in black. In both panels, $M_{\bullet} = 10^6M_{\odot}$, $r_{\text{infl}} = 0.761$ pc, and $m_{\star} = 1M_{\odot}$.

holes is given by:

$$\dot{N}_{\text{TC}} = 2\pi^2 \int_0^{v_{\text{esc}}} \int_0^{v_{\text{esc}} \sqrt{v_{\text{esc}}^2 - v_{\parallel}^2}} V_0 r_o^2 \left[1 + 2 \frac{G(m_{\star} + m_{\text{bh}})}{r_o V_0^2} \right] f_{\text{bh}}(v) v_{\perp} dv_{\perp} dv_{\parallel} \quad (31)$$

where

$$V_0 = \sqrt{(V - v_{\parallel})^2 + v_{\perp}^2} \quad (32)$$

$$r_0 = \max[r_{\text{capt}}(V_0, m_{\text{bh}}/m_{\star}), r_{\text{t}}]$$

For practical evaluation, the tidal capture rate is orbit averaged following Eq. A2.

2.5 Comparison between the different close encounters

Given the many close encounters at play in a galactic nucleus, it is useful to compare their relative rates. We perform this comparison in Fig. 1, which illustrates how strong scattering rates and other encounter rates vary as one changes

stellar eccentricity e , and various properties of the central cusp (e.g. γ_{\star} , γ_{bh}). The rate of angular momentum relaxation,

$$\dot{N}_{\text{AM}} \sim \mu(\epsilon)(1 - e^2) \quad (33)$$

with $\mu(\epsilon)$, the diffusion coefficient as computed in Eq. 35 is also plotted as a useful reference rate: loss cone shielding is likely to only become important insofar as the rate of a destructive close encounter can become comparable to \dot{N}_{AM} . Note that here t_r is the energy relaxation time, $\langle m_{\star}^2 \rangle$ is the second moment of the stellar mass function, n_{\star} is the stellar number density, the Coulomb logarithm $\ln \Lambda \approx \ln(0.4M_{\bullet}/m_{\star})$, and in general Eq. ?? is approximate⁵. Notably, it is a single-species relaxation time, although it can be generalized straightforwardly to a multi-species cusp.

We see that in general, $\dot{N}_{\text{AM}} \gg \dot{N}_{\text{ej}}$ so long as the relevant power-law indices $\gamma \lesssim 2$. In contrast, $\gamma = 5/2$ leads to ejection rates at large a that can exceed \dot{N}_{AM} . At small a , ejection rates decline and can be exceeded by close encounter rates, but regardless of γ and a , $\dot{N}_{\text{AM}} \gg \dot{N}_{\text{ce}}$ always.

To summarize, these simple rate comparisons show that (i) destructive close encounters will never effectively shield the loss cone; (ii) ejections in strong scatterings are likely to shield the loss cone for $a \sim r_{\text{infl}}$ and $\gamma > 2$; (iii) at $a \ll r_{\text{infl}}$, strong scatterings become subdominant to close encounters as a way to remove stars from the distribution function. Ultimately, however, these rate comparisons only provide an order of magnitude check of the competition between different physical processes, so we now move on to computing time-dependent solutions to the loss cone problem in the presence of strong scattering and close encounters.

3 THE SHIELDED LOSS CONE

3.1 Loss Cone Theory

The radial distribution of stars and compact objects evolves over time due to two-body relaxation. In the continuum limit, and assuming spherical symmetry, the stellar population is represented with a distribution function $f(\epsilon, J)$, where J is the specific angular momentum of a stellar orbit. For the near-radial orbits relevant for TDEs, angular momentum relaxation is much faster than energy relaxation and we will use a two-timescale argument: we separate $f(\epsilon, J) = f_{\epsilon}(\epsilon)f_j(J)$ and assume a frozen distribution of energy. By assumption, stars are fixed in bins of orbital energy, but allowed to diffuse through angular momentum space in a random walk. This process is captured by the orbit-averaged Fokker-Planck equation (Merritt & Wang 2005),

$$\frac{\partial f}{\partial \tau} = \frac{1}{4j} \frac{\partial}{\partial j} \left(j \frac{\partial f}{\partial j} \right) \quad (34)$$

where $j \equiv J/J_c(\epsilon) = \mathcal{R}^{1/2}$ is a dimensionless angular momentum variable (normalized by the angular momentum of a circular orbit, J_c) and $\tau \equiv \mu(\epsilon)t \approx t/t_r$ is a dimensionless version of time t , with $\mu(\epsilon)$ the orbit-averaged diffusion coefficient defined more precisely in §3.

⁵ In Fig. ??, we actually plot a more precise $\dot{N}_{\text{AM}} = \mu/(1 - e^2)$, where μ is an orbit-averaged angular momentum diffusion coefficient defined more precisely in §3.

coefficient at specific energy ϵ :

$$\mu(\epsilon) = \frac{1}{P(\epsilon)} \oint \frac{dr}{v_r} \lim_{\mathcal{R} \rightarrow 0} \frac{\langle (\Delta\mathcal{R})^2 \rangle}{2\mathcal{R}}. \quad (35)$$

Here $P(\epsilon)$ is the orbital period of a radial orbit of energy ϵ , v_r is the star's radial velocity, and the local diffusion coefficient $\langle (\Delta\mathcal{R})^2 \rangle$ is presented in Appendix B. Hence, $\tau \approx t/t_r$, with t_r , the energy relaxation time..

In the presence of strong scatterings and destructive close encounters, stars can be ejected or otherwise removed from the distribution, which we model by adding a sink term to the Fokker-Planck equation:

$$\frac{\partial f}{\partial \tau} = \frac{1}{4j} \frac{\partial}{\partial j} \left(j \frac{\partial f}{\partial j} \right) - \frac{\langle \dot{N}_{ej} \rangle}{\mu(\epsilon)} f. \quad (36)$$

Here $\langle \dot{N}_{ej} \rangle$ is the orbit-averaged rate of close encounters, as derived in section 2.2 for strong scattering and 2 for other close encounters.

The initial and boundary conditions depend on a dimensionless diffusivity parameter $q(\epsilon) = \mu(\epsilon)P(\epsilon)/\mathcal{R}_{LC}(\epsilon)$, which is defined in terms of the size of the loss cone in dimensionless angular momentum space ($\mathcal{R}_{LC} \approx 2GM R_t$). The value of q determines whether the loss cone evolves in the “empty” ($q \ll 1$; stars immediately destroyed once $\mathcal{R} \leq \mathcal{R}_{LC}$) or “full” ($q \gg 1$; stars may move in and out of the loss cone multiple times per orbit) limits. When $q(\epsilon) \ll 1$, one can assume an absorbing boundary condition at the loss cone, and a zero-flux boundary condition at $j = 1$:

$$f(j \leq j_{LC}, t) = 0; \quad \left. \frac{\partial f}{\partial j} \right|_{j=1} = 0. \quad (37)$$

Conversely, when $q(\epsilon) \gg 1$, the distribution function does not go to zero until a much smaller value of dimensionless angular momentum, $j_0(\epsilon)^2 = \mathcal{R}_0(\epsilon) = \mathcal{R}_{LC}(\epsilon) \exp(-q/\xi(q))$, where

$$\xi(\epsilon) \approx (q^2 + q^4)^{1/4} \quad (38)$$

is an approximate flux variable that smoothly bridges the empty and full loss cone limits. We thus have a more general set of boundary conditions that we use for all numerical solutions:

$$f(j \leq j_0, t) = 0; \quad \left. \frac{\partial f}{\partial j} \right|_{j=1} = 0. \quad (39)$$

In both cases we take as an initial condition an isotropic distribution, $f(j) = 1$, for $j_0 \leq j \leq 1$, and set $f(j) = 0$ elsewhere.

The flux of stars that scatter into the loss cone per unit time and energy is given by:

$$\mathcal{F}(t; \epsilon) = 2\pi^2 \mu(\epsilon) P(\epsilon) J_c^2(\epsilon) f_\epsilon(\epsilon) \left(j \frac{\partial f_j(j, t)}{\partial j} \right)_{j=j_{LC}}. \quad (40)$$

Then, the TDE rate is obtained by integrating $\mathcal{F}(\epsilon)$ across many bins of energy ϵ , such as :

$$\dot{N}_{TDE}(t) = \int \mathcal{F}(t; \epsilon) d\epsilon. \quad (41)$$

3.2 Numerical Results

We begin by solving the modified Fokker-Planck equation (Eq. 36) numerically. An example of these time-dependent

solutions is presented in Fig. 2, where we show the evolution of the angular momentum distribution (in a bin of fixed ϵ), both with and without strong scatterings. In the absence of strong scatterings, we see that we quickly achieve the logarithmic Cohn-Kulsrud profile (Cohn & Kulsrud 1978). However, when strong scatterings are turned on, a range of outcomes are possible. For ($\gamma_* = 3/2$ and $\gamma_{bh} = 2$), both stars and sBHs have very small impact at early times and a moderate one at later times. For $\gamma_{bh} = 5/2$ or an ultrasteep density star profiles ($\gamma_* = 5/2$, the distribution function can be radically modified relative to the standard Cohn-Kulsrud solution, with a major depletion of low- j orbits. The “cavity” carved out of the distribution function at low j in this case reflects the impact of strong scattering, which preferentially ejects stars on the most radial orbits (as it is generally the case that ejection rates for an individual star are pericenter-dominated, see e.g. Eq. 13).

When strong scatterings are capable of strongly depleting the low- j end of the distribution function, the result is a major reduction in loss cone flux (as $\mathcal{F} \propto (\partial f_j / \partial j)|_{j=j_{LC}}$). We further explore this effect by computing flux reduction for different black hole slopes and black hole mass, applying Eq. 40 to our numerical solutions, and plot the results in Fig. 2. In this figure, we see that in all cases, there is relatively little evolution of the flux suppression factor $\mathcal{F}/\mathcal{F}_w$ (here \mathcal{F}_w is the flux into the loss cone that would be achieved without the presence of strong scatterings). Suppression factors $\mathcal{F}/\mathcal{F}_w$ are modest ≈ 1 for $\gamma_{bh} = 2$, reach the factor-of-2 level for $\gamma_{bh} = 9/4$, and can produce multiple-order-of-magnitude drops in the TDE rate for steeper γ_{bh} values. In agreement with Eq. 13, we see stronger levels of flux suppression for larger values of m_{bh} .

3.3 Analytical solutions of Fokker-Planck with strong scattering

The flux of stars inside the loss cone $\mathcal{F}(\epsilon)$ is a sharply peaked function, and most of the stars come from energies close to the influence radius. As we have shown, in section 2, the dominant close-encounter mechanism at influence radius is strong scattering. Therefore, we searched for an analytical solution to the Fokker-Planck equation with a sink term corresponding to strong scattering (Eq. 36).

3.3.1 Equal mass scatterer

For an equal mass scatterer, we found an exact analytical form for the orbit-averaged ejection rate for all relevant integer or half-integer values of γ_* . The formulas for $\gamma_* = 3/2, 5/2$ can be found in Appendix A.⁶ Then, using the method of Frobenius, we derived an analytic, time-dependent solution to the modified Fokker-Planck equation for these two power-law distributions. For the shallower slope, $\gamma_* = 3/2$, the solution is very close to the Cohn-Kulsrud profile, whereas for the steeper slope of $\gamma_* = 5/2$, it has an exponential behaviour. The solutions for $\gamma_* = 3/2$ and $\gamma_* = 5/2$ can be written

⁶ Formulas for $\gamma_* = 2$ are in close form with Hypergeometrics series

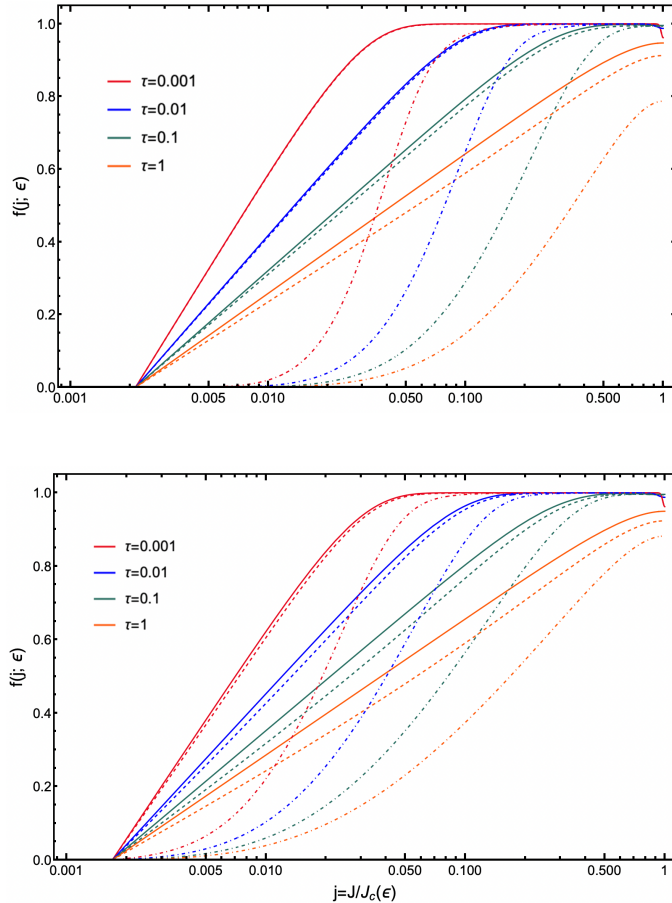


Figure 2. Numerical evolution of the distribution function $f(j; \epsilon)$ as a function of the dimensionless angular momentum j at fixed energy ϵ corresponding to $a = r_{inf}$, shown for different snapshots in dimensionless time, τ , for a Milky Way-like galaxy ($M = 4 \times 10^6 M_\odot$). The solid lines correspond to the evolution without strong scattering or other sink terms (Eq. 34). *Top*: strong scattering (Eq. 36) from stars only; dashed lines show $\gamma_* = 3/2$, dot-dashed lines $\gamma_* = 5/2$. *Bottom*: strong scattering from black holes; dashed lines show $\gamma_{bh} = 2$, dot-dashed lines $\gamma_{bh} = 5/2$. In this panel $\gamma_* = 3/2$, $N_{bh} = 10^3$, and $m_{bh} = 30M_\odot$. In both panels we see dramatic changes to the distribution f for ultra-steep density cusps, but only minor changes for more shallow profiles.

explicitly as:

$$f_{3/2}(j) = (1 + 16A_j)(a + b \ln j) - 32A_j \quad (42)$$

$$f_{5/2}(j) = e^{-\frac{8\sqrt{2A}}{\sqrt{j}}} j^{1/4} [ag_-(j) + be^{\frac{16\sqrt{2A}}{\sqrt{j}}} g_+(j)]$$

where $A = \langle \dot{N}_{ej} \rangle / \mu(\epsilon)$ is a per-star sink term, $\langle \dot{N}_{ej} \rangle$ can be found in Appendix A, and two undetermined constants $-b$ and a need to be found. These solutions are valid at small j , but breaks down at $j \sim 1$. Their explicit time-dependence comes from the undetermined constants a and b . In practice, b is deterministically set as a function of a using the absorbing boundary condition at $j = j_0$, so there is only one true time-dependent free parameter. We find that a depends on the dimensionless time τ as $a \sim \tau^{-1/2}$. Since the approximate time-scale for angular momentum relaxation to occur is $t_j(j) \sim j^2 t_r$, our solution is accurate for $j \lesssim j_{CK} = \sqrt{\tau}$

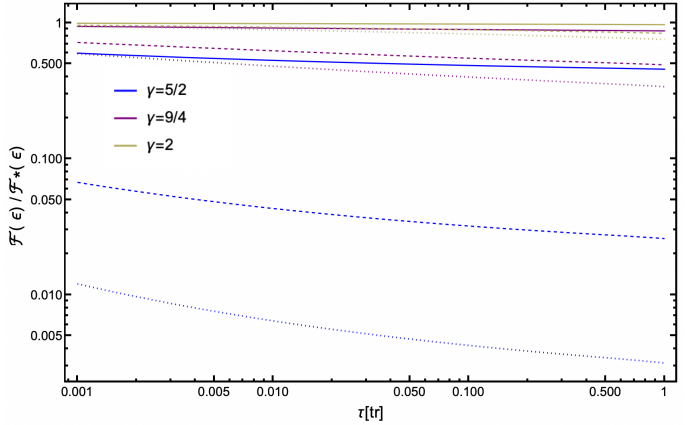


Figure 3. Evolution of the flux of stars inside the loss cone with strong scattering (\mathcal{F}) divided by the flux of stars neglecting strong scattering (\mathcal{F}_w) as a function of dimensionless time τ at fixed energy ϵ , for a Milky Way like galaxy with $m_* = 1$, $\gamma_* = 3/2$, $N_{bh} = 10^3$. Different colors correspond to different stellar mass black hole density slopes γ_{bh} (see legends). Full lines show $m_{bh} = 10M_\odot$, dashed lines show $m_{bh} = 30M_\odot$, and dot-dashed lines $m_{bh} = 50M_\odot$ stars.

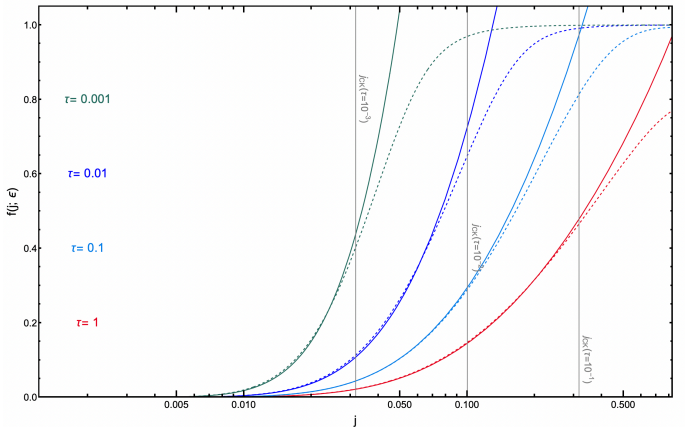


Figure 4. Evolution of the distribution function $f(j; \epsilon)$ as a function of the dimensionless angular momentum j at fixed energy ϵ , shown for different snapshots in dimensionless time, τ . Here $\gamma_* = 5/2$ and we consider a single-mass stellar population. The dashed curves show numerical solutions of the 1D Fokker-Planck equation and solid lines show the approximate analytic solution obtained from the method of Frobenius in Eq. 42. The agreement is excellent for values of $j \lesssim j_{CK}$, the ‘‘Cohn-Kulsrud’’ angular momentum below which the distribution function has had time to relax into a QSS.

(Stone et al. 2018). In Fig. 4, the numerical solutions of the Fokker-Planck equation with strong scatterings (Eq. 36) are compared to our analytical solution ($\gamma_* = 5/2$) at different dimensionless times. The agreement is excellent for values of $j \lesssim j_{CK}$, the ‘‘Cohn-Kulsrud’’ angular momentum below which the distribution function has had time to relax into a QSS.

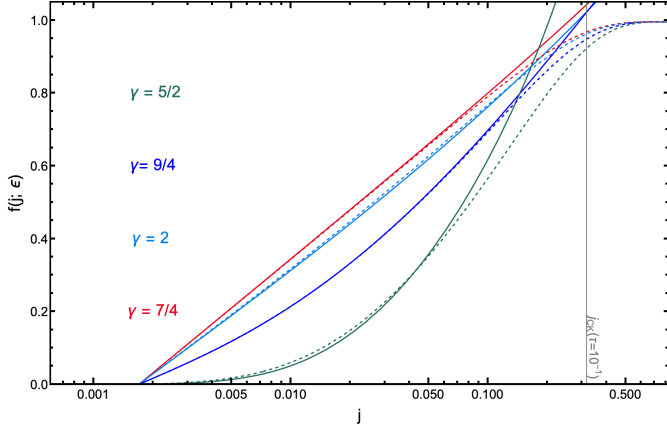


Figure 5. Evolution of the distribution function $f(j; \epsilon)$ as a function of the dimensionless angular momentum j at fixed energy ϵ , at dimensionless time, $\tau = 0.1$ for different slopes of the black holes. Here $\gamma_* = 3/2$, the stellar mass black holes have a mass $m = 30M_\odot$, and different colors correspond to different sBH slopes γ_{bh} (see labels in figure). The dashed curves show numerical solutions of the 1D Fokker-Planck equation and solid lines show the approximate analytic solution obtained from the method of Frobenius in Eq. 43. As in Fig. 4, the agreement is again excellent for values of $j \lesssim j_{\text{CK}}$.

3.3.2 Unequal mass scatterer

For an unequal mass scatterer, we found close form solutions for the local rates and derived approximate solutions for the orbit-averaged rates. We then repeat our application of the Frobenius method to find time-dependent solutions for physically motivated slopes. Specifically, we find solutions for the time evolution of the distribution function of stars scattering off a population of sBHs with power-law slopes of indices $\gamma_{\text{bh}} = 3/2, 7/4, 2, 9/4$ and $5/2$. The resulting closed form solutions are as follows:

$$\begin{aligned}
 f_{3/2,u}(j) &= (1 + 4Aj)(a + b \ln j) - 8Ajb \\
 f_{7/4,u}(j) &= (1 + 8A\sqrt{j})^2 \left(a - \frac{b}{2}(2 \ln 16A + \ln j) \right) \\
 &\quad - 2b(\gamma_E + 16A(-1 + \gamma_E)\sqrt{j} + 32A^2(-3 + 2\gamma_E)j) \\
 f_{2,u}(j) &= j^{-2\sqrt{A}}(j^{4\sqrt{A}}a + b) \\
 f_{9/4,u} &= e^{-8\sqrt{A}j^{-1/4}}j^{1/8} \left(\frac{\sqrt{\pi}b}{2A^{1/4}}(-1 + \frac{j^{1/4}}{64A^{1/2}}) \right. \\
 &\quad \left. + \frac{a}{2\sqrt{2\pi}}\cosh(8\sqrt{A}j^{-1/4}) \right) \\
 f_{5/2,u}(j) &= e^{\frac{-4\sqrt{A}}{\sqrt{j}}}j^{1/4}[ah_-(j) + be^{\frac{8\sqrt{A}}{\sqrt{j}}}h_-(j)]
 \end{aligned} \tag{43}$$

where γ_E is Euler's constant and $h_{\pm} = 1 \pm \frac{\sqrt{j}}{32\sqrt{A}} + 0.0044\frac{j}{A}$. As before, explicit time-dependence enters through two undetermined coefficients, a and b , although application of the absorbing inner boundary condition allows us to eliminate one of these. We find that the remaining coefficient can be determined quite accurately with a matching procedure: we set the value of our solution, $f_{\gamma_{\text{bh}},u}(xj_{\text{CK}})$ equal to the value of the Cohn-Kulsrud distribution at $j = xj_{\text{CK}}$. Here x is a

dimensionless number of order unity; we find that $x \sim 0.1$ yields a good match.

In Fig. 5, we compare the analytical solutions we obtained for unequal-mass strong scatterings at various γ_{bh} with the numerical solutions to Eq. 36. In all cases (analytic and numerical) the comparison is done at a fixed dimensionless time $\tau = 0.1$. As can be seen, the agreement between analytical and numerical solutions is excellent for $j \lesssim \sqrt{\tau}$.

4 IMPACT ON TDE RATES

As we have seen in Fig. 3, the flux inside the loss cone reaches a quasi-stationary state after a time $t \sim 0.1 t_r$, with t_r , the relaxation time. Therefore, in this section we explore the impact on TDE rates of strong scattering after a time where the quasi-stationary state has been reached. To compute numerical fluxes we compute the diffusion coefficients $\mu(\epsilon)$ for a grid of energies. Equation 36 is then integrated forward for the appropriate dimensionless time at each ϵ -value and the flux computed from equation 40. Finally, TDE rates are obtained by integrating across the energy bins, equation 41. To compute analytical fluxes, we use our solutions presented in Sec 3.3 for the appropriate dimensionless time at each ϵ -value, then compute the fluxes with equation 40 and finally integrate across multiple energy bins to obtain TDE rates, equation 41.

4.1 Rates

In Fig. 6, we show energy-integrated TDE rates as a function of MBH mass both with and without the effects of strong scattering for cusp galaxies with radius of influence $r_{\text{infl}} = 11 \text{ pc} \left(\frac{M_\bullet}{10^8 M_\odot} \right)^{0.58}$ (Stone & Metzger 2016).

We can note that our TDE rates without strong scattering shown in Fig. 6 are a factor of a few higher than in previous loss cone calculations (Wang & Merritt 2004; Stone & Metzger 2016). This effect is due to the inclusion of stellar mass black holes. Indeed, stellar mass black holes dominate the total relaxation rate and increase diffusion coefficients hence increasing the TDE rates by a factor of a few. This effect is further explored in Fig. 7 where we show the influence of different sBH masses on TDE rates both with and without strong scattering.

We see here that the effects of strong scattering are quite modest for $\gamma_{\text{bh}} = 2$ (reducing TDE rates by $\lesssim 50\%$), rise to a factor of 2 reduction for $\gamma = 9/4$, and then become very large (at least an order of magnitude reduction) for $\gamma = 5/2$. It is important to note, that the TDE rates we obtain with $\gamma_{\text{bh}} = 5/2$ are in agreement with the observed TDE rates. In this example we have taken $m_{\text{bh}} = 30M_\odot$; smaller (larger) sBHs would produce a smaller (larger) loss cone shielding effect.

In Fig. 7, we show that in the absence of strong scattering, TDE rates increase by a factor ≈ 3 as m_{bh} increases from $10M_\odot$ to $50M_\odot$. In the presence of strong scattering, however, the TDE rate is substantially lower at all values of sBH mass and is relatively independent of m_{bh} . Although larger m_{bh} values still increase diffusion coefficients, this is offset by the greater rate at which stars are ejected in close encounters (note that both effects scale $\propto m_{\text{bh}}^2$).

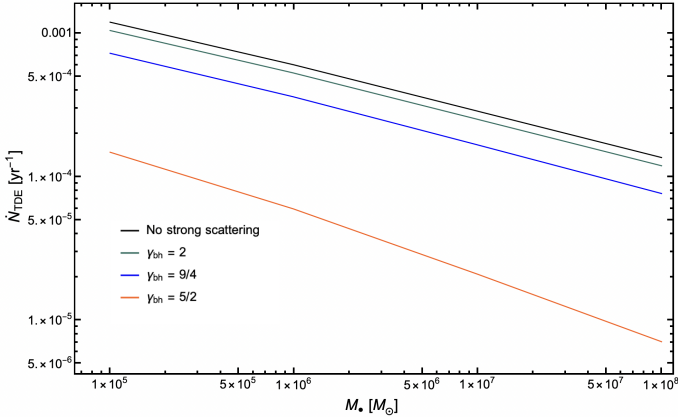


Figure 6. Tidal disruption rates \dot{N}_{TDE} measured in units of stars per year with (colored curves) and without (black curve) strong scattering. Results are plotted against MBH mass M_{\bullet} , with the following parameters: $m_{\star} = 1M_{\odot}$, $\gamma_{\star} = 3/2$, $m_{\text{bh}} = 30M_{\odot}$ and different sBH density profile slopes: in particular, we show $\gamma_{\text{bh}} = 2$, $\gamma_{\text{bh}} = 9/4$, and $\gamma_{\text{bh}} = 5/2$ as green, blue, and orange curves, respectively. Reductions in total TDE rates begin to become significant for $\gamma_{\text{bh}} \geq 9/4$.

In these calculations, we considered a broad range of sBH masses, from $m_{\text{bh}} = 5M_{\odot} - 50M_{\odot}$. Here we are motivated partially by the “initial mass function” for sBHs formed via the deaths of massive stars. Depending on the metallicity of the stellar population, the maximum masses for sBHs formed in this way is likely to be $\approx 50M_{\odot}$ (Spera & Mapelli 2017), although even with a favorable metallicity, the large majority of sBHs will have substantially lower masses⁷. However, once a population of sBHs is situated in a galactic center environment, it may be able to gain mass through mergers and accretion. Most notably, any episode of large-scale MBH accretion will grind down and capture many of the pre-existing sBHs into the MBH accretion disk (Syer et al. 1991); once embedded in this disk, they can be processed to larger masses either via mergers (Bellovary et al. 2016; Tagawa et al. 2020) or from direct gas accretion (Gilbaum & Stone 2022). After the AGN episode ends, the population may relax into a more spherical configuration of the type we assume here (although see Szölgyén & Kocsis 2018). Efficient sBH growth through merger may also occur during periods of time when a dense nuclear star cluster lacks a MBH (Antonini & Rasio 2016), either early during its evolution or at later points if an MBH is temporarily ejected via gravitational wave recoil (Gualandris & Merritt 2008).

The rate suppression due to strong scatterings can depend strongly on the semimajor axis, or equivalently the energy ϵ , of the stars in question. At low values of ϵ , TDE rates can be suppressed by one or more orders of magnitude in the presence of high-mass and steeply cusped sBHs, but the suppression is often milder (especially at high γ_{bh}) for the subset of stars on tightly bound, high- ϵ orbits. We have seen this numerically, but it can also be understood analytically via Eqs. 12 and 13. A consequence of this is that galactic nu-

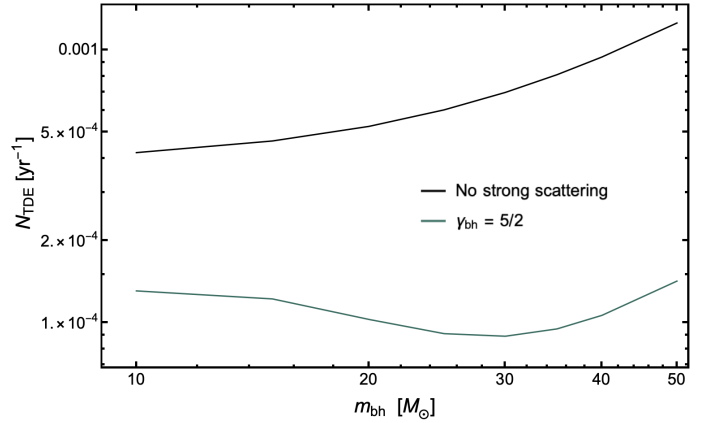


Figure 7. Tidal disruption rates \dot{N}_{TDE} measured in units of stars per year with (colored curves) and without (black curve) strong scattering as a function of stellar black hole mass m_{bh} . Higher stellar mass black holes increase the diffusion coefficients and hence the TDE rates without strong scattering. However, with strong scattering there is a balance between the effect on the diffusion and the higher efficiency at removing stars of heavier sBHs.

clei can see a relative suppression of high- β TDEs, which are overwhelmingly produced in the full loss cone (or “pinhole”) regime where rates are suppressed most heavily by strong scatterings (Stone & Metzger 2016). Although the observational implications of high- vs low- β TDEs are not yet clear, high- β events may exhibit faster circularization (Hayasaki et al. 2013; Bonnerot et al. 2016), produce stronger thermal soft X-ray emission (Dai et al. 2015), produce stronger sub-relativistic outflows from the circularization process (Metzger & Stone 2016; Lu & Bonnerot 2020). These observational signatures would be less frequently produced in galaxies with large and steeply cusped populations of sBHs.

We quantify this effect in Fig. 8, which shows f_{pinhole} , the fraction of TDEs occurring in the pinhole regime, as a function of MBH mass M_{\bullet} (with and without strong scattering). Without strong scattering, the value of f_{pinhole} decreases with increasing M_{\bullet} and drops steeply for $M_{\bullet} \sim 10^8M_{\odot}$, as expected for cusp galaxies. Interestingly, the influence of strong scattering modifies the pinhole fraction in two opposite directions, with the net effect depending on γ_{bh} . The first effect is already explained in the preceding paragraph: at fixed τ , loss cone flux is more greatly reduced (by strong scatterings) when ϵ is low than when ϵ is high. However, a countervailing force is visible in Fig. 2, where we see the mild but relevant time evolution of the suppression due to strong scatterings. The suppression factor $\mathcal{F}(\epsilon)/\mathcal{F}_w(\epsilon)$ becomes smaller and smaller as τ grows, so when computing an energy-integrated \dot{N}_{TDE} rate, the bins of large ϵ (with larger τ) will be further along the time evolution of their suppression curves. In Fig. 8, we see that for large γ_{bh} , the first effect wins out and the pinhole fraction decreases due to ejections. But for $\gamma_{\text{bh}} \lesssim 9/4$, the second effect wins out and the pinhole fraction sees little net change from strong scatterings (the net change that does exist is a very mild increase in f_{pinhole}).

⁷ We note that this type of calculation is quite sensitive to uncertain prescriptions for line-driven wind mass loss (Belczynski et al. 2010).

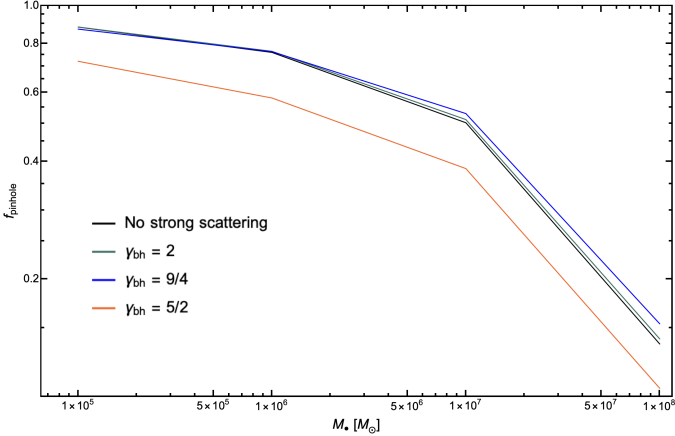


Figure 8. The fraction, f_{pinhole} , of all TDEs in a galaxy which fall into the pinhole regime of tidal disruption, plotted against MBH M_{\bullet} . The black curve shows this dependence without strong scattering, while the colored curves show the pinhole fraction in the presence of strong scattering (see labels in-panel). TDEs in the pinhole (or full loss cone) regime can access any β , while TDEs in the opposite, diffusive, regime, almost always have $\beta \approx 1$.

4.2 E+A preference

Observations have revealed that E+A and other post-starburst galaxies are significantly over-represented among TDE hosts (Arcavi et al. 2014; French et al. 2016, 2017; Law-Smith et al. 2017; Graur et al. 2018; French et al. 2020; Hammerstein et al. 2021). A few solutions have been proposed to explain this preference: stellar overdensities (Stone et al. 2018), radial anisotropies (Stone et al. 2018), SMBH binaries (e.g Arcavi et al. 2014) and accounting for a complete stellar mass function (Bortolas 2022).

In the framework of our revised loss cone theory, we have shown that steep slopes induce a strong reduction of TDE rates. Motivated by our findings, here we study the impact of stellar overdensities with strong scattering. In this section, we consider only stars and no sBHs.

E+A galaxies are post-starburst galaxies. If we assume that most of the central stars formed impulsively in a starburst, these ultrasteep stellar central density cusps will relax over time towards a steady state configuration: the Bahcall–Wolf cusp, with $\gamma_{\star} = 7/4$ (Bahcall & Wolf 1976b). An ultrasteep stellar density profile will result in much shorter relaxation times, especially at small energies, and hence the relaxation to a BW cusp is quicker for steeper star profiles. Following Stone et al. (2018), we define the Bahcall–Wolf radius r_{BW} as the radius where the post-starburst age t equals the local energy relaxation time:

$$r_{\text{BW}} = \left(\frac{M_{\bullet}^{3/2} \langle m_{\star} \rangle}{G^{1/2} \langle m_{\star}^2 \rangle \rho_{\text{infr}} r_{\text{infr}}^{\gamma} t \ln \Lambda} \right)^{\frac{1}{3/2 - \gamma}} \quad (44)$$

In Fig. 9, we plot the Bahcall–Wolf radius r_{BW} divided by the influence radius for different MBH masses. As r_{BW} expands, energy relaxation erodes the population of the most tightly bound stars, decreasing their density relative to the initial conditions. The density decrease at high ϵ reduces the efficiency of loss cone shielding, as it is the most tightly bound stars which are responsible for the strongest shielding effects. From Fig. 9, we see that this cusp erosion is fastest

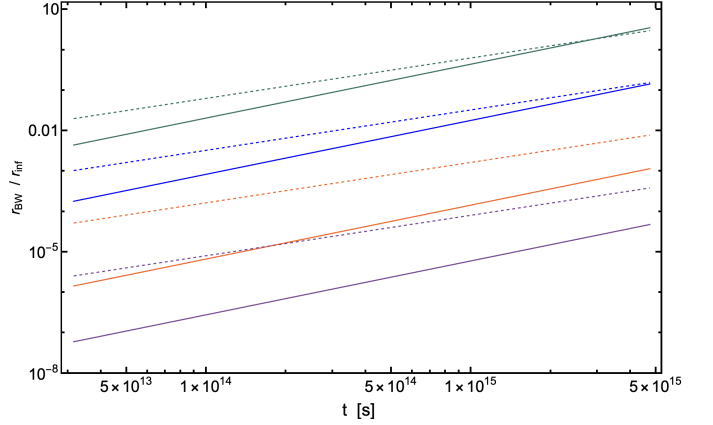


Figure 9. Time evolution of the Bahcall–Wolf radius divided by the radius of influence for different MBH masses. Green, blue, orange, and purple lines correspond to $M_{\bullet} = 10^5 M_{\odot}$, $M_{\bullet} = 10^6 M_{\odot}$, $M_{\bullet} = 10^7 M_{\odot}$, and $M_{\bullet} = 10^8 M_{\odot}$, respectively. The dashed lines correspond to $\gamma_{\star} = 5/2$ while full lines are for $\gamma_{\star} = 9/4$.

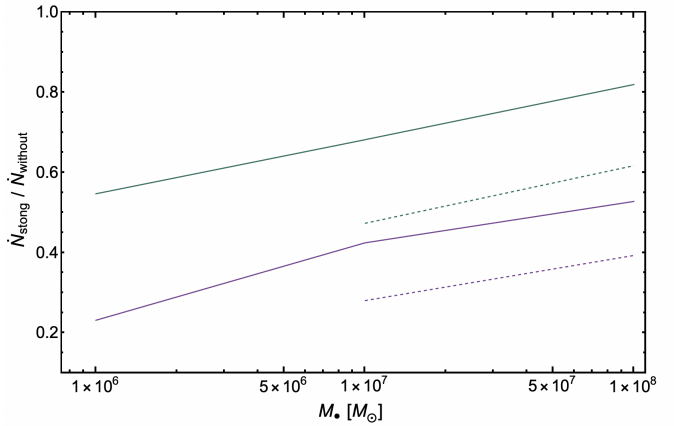


Figure 10. Rates of TDEs with strong scattering divided by the rates of TDEs without strong scattering, shown as a function of the MBH mass. Green lines are for $\gamma_{\star} = 9/4$, purple lines for $\gamma_{\star} = 5/2$. Full lines are at $t = 10$ Myr (15 Myr for $\gamma_{\star} = 9/4$), dashed lines are at $t = 100$ Myr (150 Myr for $\gamma_{\star} = 9/4$).

for small MBHs and slowest for large MBHs. As we do not self-consistently model this cusp erosion in our calculations, we compute TDE rate reductions at times where this effect would be minor. Indeed, when cusp erosion starts to be significant, ultrasteep stellar profiles will not be able to ‘self-shield’ unless new stars are being continuously deposited at small radii (e.g. by the Hills mechanism).

In Fig. 10, we show TDE rates with strong scattering normalized by TDE rates without strong scattering, as a function of MBH masses. We neglect the smallest MBH masses where flattening of the inner profile may be most relevant. We find that strong scatterings can reduce the TDE rate by up to an order of magnitude depending on the stellar slope and MBH mass, showing that ultrasteep stellar profiles may efficiently self-shield, reducing the otherwise high TDE rates they would produce.

5 DISCUSSION & CONCLUSIONS

In this paper, we have proposed a revised loss cone theory that takes into account both classical weak scattering and close encounters: strong scattering, collisions, tidal captures and μ -TDEs. These close encounters can occur at non-negligible rates inside the radius of influence, where stellar densities can be higher than anywhere else in the universe. Below we summarize our key findings:

- (i) For stars with semi-major axis $a \sim r_{\text{inf}}$, i.e. the primary sources of TDEs, strong scattering rates are significantly larger than other close encounter rates. For very high orbital energies, collisions become the dominant close encounter. However, those energies have a very small contribution to TDE rates.
- (ii) We derive time-dependent analytical solutions of the Fokker-Planck equation with strong scattering for a broad range of physically motivated slopes. This family of analytic solutions, which we can write in closed form for all relevant integer, half-integer, and quarter-integer γ values, is a generalization of the standard [Cohn & Kulsrud \(1978\)](#) $f(j)$ distribution function in the presence of strong scatterings.
- (iii) We find that for black hole slopes $\gamma_{\text{bh}} \geq 9/4$, the loss cone will be effectively shielded by strong scattering. TDE rates are reduced by a factor ~ 2 for $\gamma_{\text{bh}} = 9/4$ and by a factor ≥ 10 for $\gamma_{\text{bh}} = 5/2$.
- (iv) Strong scattering is more effective at removing stars with $a \sim r_{\text{inf}}$ compared to stars with $a \ll r_{\text{inf}}$. Thus, in addition to shielding the loss cone, strong scattering can also reduce the fraction of TDEs in the pinhole regime, and therefore the fraction of deeply plunging TDEs for $\gamma_{\text{bh}} = 5/2$.
- (v) Stellar overdensities, a widespread explanation for the E+A preference among TDEs, is challenged by our revised loss cone theory. Indeed, in classical loss cone theory, ultra steep stellar slopes enhance the diffusion coefficients and, hence the TDE rates. However, we have shown that they also enhance the rates of strong scattering and hence reduce TDE rates. The net TDE enhancement may therefore be mild.

In this paper, we have focused on the most dramatic qualitative difference between weak and strong scatterings: ejection. However, stars also have milder but still strong encounters that can non-diffusively move them to new – but still bound – energies. This effect will be the subject of a future work. The shielding effect we have studied depends on black hole slopes which have not been constrained observationally. N -body simulations have shown that sBHs can settle to a slope of $\gamma_{\text{bh}} \geq 2$ ([Amaro-Seoane & Pretor 2011](#); [Pretor & Amaro-Seoane 2010b](#)), in agreement with some predictions of strong mass segregation ([Alexander & Hopman 2009](#)). Moreover, [Generozov et al. \(2018\)](#) showed that, in the presence of a source term that is continuously depositing new stars or sBHs at small radii, black holes will settle into a density profile with $\gamma_{\text{bh}} = 5/2$. Motivated by these studies, we considered different black hole slopes with $\gamma_{\text{bh}} \leq 2.5$.

If steep profiles for black holes are common in galactic nuclei, this may explain persistent discrepancies between the high predicted rates of TDEs ([Wang & Merritt 2004](#)) and the (relatively) low observed rates of TDEs in low-mass galactic nuclei. While the steep TDE luminosity function ([van Velzen 2018](#)) helps to resolve this rate discrepancy, it may be unable

to resolve the entire breadth of the discrepancy if the occupation fraction of small MBHs ($\sim 10^5 M_{\odot}$) is high in dwarf galactic nuclei. Conversely, loss cone shielding may pose a challenge for the “overdensity” solution ([Stone & Metzger 2016](#); [Stone & van Velzen 2016](#); [Stone et al. 2018](#)) to the observed post-starburst preference ([Arcavi et al. 2014](#); [French et al. 2016, 2017](#); [Hammerstein et al. 2021](#)) among the host galaxies of TDEs. While an ultrasteep stellar distribution can boost TDE rates up to a point, our work here shows that the gains from increasing γ_{\star} beyond $9/4$ may be self-limiting, and that TDE rates may even drop as γ_{\star} increases to very large values.

It is worth mentioning that we considered a monochromatic distribution of stars throughout the paper. However, we did also compute the impact of a Kroupa IMF and found that it increased all TDE rates with and without strong scattering by a common factor of 1.6. It is also possible that shielding effects could be important for the production of hypervelocity stars in binary breakups ([Hills 1988](#)), as these are generally sourced from binaries with galactocentric semimajor axes $a \gg r_{\text{inf}}$ ([Perets et al. 2007](#)).

To conclude, we emphasize that we considered the 1D Fokker-Planck equation in angular momentum, neglecting energy evolution of the stellar (and sBH) distribution function. This may be important for steep density profiles that are not quasi-steady states. This, together with the effect of strong scattering that can non-diffusively move stars to higher energies will be the subject of a future work.

ACKNOWLEDGEMENTS

We thank Luca Broggi for helpful discussions. OT is grateful for the Einstein-Kaye scholarship. This work was partially funded by the Israel Science Foundation (Individual Research Grant 2565/19) and the United States-Israel Binational Science Foundation (Grant No. 2019772).

REFERENCES

- Alexander T., Hopman C., 2009, [ApJ](#), **697**, 1861
- Amaro-Seoane P., Pretor M., 2011, [Classical and Quantum Gravity](#), **28**, 094017
- Antonini F., Rasio F. A., 2016, [ApJ](#), **831**, 187
- Arcavi I., et al., 2014, [ApJ](#), **793**, 38
- Bade N., Komossa S., Dahlem M., 1996, [A&A](#), **309**, L35
- Bahcall J. N., Wolf R. A., 1976a, [ApJ](#), **209**, 214
- Bahcall J. N., Wolf R. A., 1976b, [ApJ](#), **209**, 214
- Bahcall J. N., Wolf R. A., 1977, [ApJ](#), **216**, 883
- Belczynski K., Bulik T., Fryer C. L., Ruiter A., Valsecchi F., Vink J. S., Hurley J. R., 2010, [ApJ](#), **714**, 1217
- Bellovary J. M., Mac Low M.-M., McKernan B., Ford K. E. S., 2016, [ApJ](#), **819**, L17
- Ben-Ami S., et al., 2022, arXiv e-prints, p. [arXiv:2208.00159](#)
- Blagorodnova N., et al., 2019, [ApJ](#), **873**, 92
- Bonnerot C., Rossi E. M., Lodato G., Price D. J., 2016, [MNRAS](#), **455**, 2253
- Bortolas E., 2022, [MNRAS](#), **511**, 2885
- Bradnick B., Mandel I., Levin Y., 2017, [MNRAS](#), **469**, 2042
- Bricman K., Gomboc A., 2020, [ApJ](#), **890**, 73
- Broggi L., Bortolas E., Bonetti M., Sesana A., Dotti M., 2022, [MNRAS](#), **514**, 3270
- Chornock R., et al., 2014, [ApJ](#), **780**, 44

- Cohn H., Kulsrud R. M., 1978, *ApJ*, **226**, 1087
 Dai L., McKinney J. C., Miller M. C., 2015, *ApJ*, **812**, L39
 Evans C. R., Kochanek C. S., 1989, *ApJ*, **346**, L13
 Fabian A. C., Pringle J. E., Rees M. J., 1975, *MNRAS*, **172**, 15
 Frank J., Rees M. J., 1976, *MNRAS*, **176**, 633
 French K. D., Arcavi I., Zabludoff A., 2016, *ApJ*, **818**, L21
 French K. D., Arcavi I., Zabludoff A., 2017, *ApJ*, **835**, 176
 French K. D., Wevers T., Law-Smith J., Graur O., Zabludoff A. I., 2020, *Space Sci. Rev.*, **216**, 32
 Generozov A., Stone N. C., Metzger B. D., Ostriker J. P., 2018, *MNRAS*, **478**, 4030
 Gezari S., et al., 2012, *Nature*, **485**, 217
 Gilbaum S., Stone N. C., 2022, *ApJ*, **928**, 191
 Graur O., French K. D., Zahid H. J., Guillochon J., Mandel K. S., Auchettl K., Zabludoff A. I., 2018, *ApJ*, **853**, 39
 Gualandris A., Merritt D., 2008, *ApJ*, **678**, 780
 Hammerstein E., et al., 2021, *ApJ*, **908**, L20
 Hammerstein E., et al., 2022, arXiv e-prints, p. arXiv:2203.01461
 Hayasaki K., Stone N., Loeb A., 2013, *MNRAS*, **434**, 909
 Hénon M., 1960a, *Annales d’Astrophysique*, **23**, 467
 Hénon M., 1960b, *Annales d’Astrophysique*, **23**, 668
 Hills J. G., 1975, *Nature*, **254**, 295
 Hills J. G., 1988, *Nature*, **331**, 687
 Hinkle J. T., et al., 2021, *MNRAS*, **500**, 1673
 Holoiu T. W. S., et al., 2016, *MNRAS*, **455**, 2918
 Hung T., et al., 2017, *ApJ*, **842**, 29
 Ivezić Ž., et al., 2019, *ApJ*, **873**, 111
 Komossa S., Bade N., 1999, *A&A*, **343**, 775
 Kremer K., Lombardi J. C., Lu W., Piro A. L., Rasio F. A., 2022, *ApJ*, **933**, 203
 Law-Smith J., Ramirez-Ruiz E., Ellison S. L., Foley R. J., 2017, *ApJ*, **850**, 22
 Lee H. M., Ostriker J. P., 1986, *ApJ*, **310**, 176
 Lightman A. P., Shapiro S. L., 1977, *ApJ*, **211**, 244
 Lin D. N. C., Tremaine S., 1980, *ApJ*, **242**, 789
 Lu W., Bonnerot C., 2020, *MNRAS*, **492**, 686
 Magorrian J., Tremaine S., 1999, *MNRAS*, **309**, 447
 Merritt D., 2013, *Dynamics and Evolution of Galactic Nuclei*
 Merritt D., Wang J., 2005, *ApJ*, **621**, L101
 Metzger B. D., Stone N. C., 2016, *MNRAS*, **461**, 948
 Nicholl M., et al., 2019, *MNRAS*, **488**, 1878
 O’Leary R. M., Loeb A., 2008, *MNRAS*, **383**, 86
 Perets H. B., Hopman C., Alexander T., 2007, *ApJ*, **656**, 709
 Perets H. B., Li Z., Lombardi James C. J., Milcarek Stephen R. J., 2016, *ApJ*, **823**, 113
 Press W. H., Teukolsky S. A., 1977, *ApJ*, **213**, 183
 Preto M., Amaro-Seoane P., 2010a, *ApJ*, **708**, L42
 Preto M., Amaro-Seoane P., 2010b, *ApJ*, **708**, L42
 Rees M. J., 1988, *Nature*, **333**, 523
 Sazonov S., et al., 2021, *MNRAS*, **508**, 3820
 Spera M., Mapelli M., 2017, *MNRAS*, **470**, 4739
 Stone N. C., Metzger B. D., 2016, *MNRAS*, **455**, 859
 Stone N. C., van Velzen S., 2016, *ApJ*, **825**, L14
 Stone N. C., Küpper A. H. W., Ostriker J. P., 2017, *MNRAS*, **467**, 4180
 Stone N. C., Generozov A., Vasiliev E., Metzger B. D., 2018, *MNRAS*, **480**, 5060
 Stone N. C., Vasiliev E., Kesden M., Rossi E. M., Perets H. B., Amaro-Seoane P., 2020, *Space Sci. Rev.*, **216**, 35
 Syer D., Clarke C. J., Rees M. J., 1991, *MNRAS*, **250**, 505
 Szölgyén Á., Kocsis B., 2018, *Phys. Rev. Lett.*, **121**, 101101
 Tagawa H., Haiman Z., Kocsis B., 2020, *ApJ*, **898**, 25
 Wang J., Merritt D., 2004, *ApJ*, **600**, 149
 Weissbein A., Sari R., 2017, *MNRAS*, **468**, 1760
 Weissbein A., Sari R., 2021, *MNRAS*, **501**, 2724
 Yu Q., Tremaine S., 2003, *ApJ*, **599**, 1129
 van Velzen S., 2018, *ApJ*, **852**, 72
 van Velzen S., et al., 2011, *ApJ*, **741**, 73
 van Velzen S., Stone N. C., Metzger B. D., Gezari S., Brown T. M., Fruchter A. S., 2019, *ApJ*, **878**, 82

APPENDIX A: ORBIT-AVERAGED EJECTION RATE

Throughout this paper, we performed orbit averages of various interaction rates X in the following way:

$$\langle X \rangle = \frac{2}{P} \int_0^\pi \dot{\nu}^{-1} X d\nu. \quad (\text{A1})$$

In the special case of a Kepler potential, this simplifies to

$$\langle X \rangle = \frac{2(1-e^2)^{3/2}}{\pi} \int_0^\pi \frac{X d\nu}{(1+e \cos \nu)^2}. \quad (\text{A2})$$

We found that the orbit averaged ejection rate has an analytical form for γ_* values which are integers or half-integers. Hereafter are the analytic forms we found for interesting values of γ . For an equal mass scatterer and $\gamma_* = 3/2$, we obtained:

$$\langle \dot{N}_{\text{ej}} \rangle = \frac{2^{1/2} \pi \rho_{\text{infl}} m G^{1/2} r_{\text{infl}}^{3/2} (4 - 3(1-e^2)^{1/2})}{(\gamma_* + 1) M^{3/2} (1-e^2)^{1/2}}. \quad (\text{A3})$$

For an equal mass scatterer, with $\gamma_* = 5/2$, we obtained:

$$\langle \dot{N}_{\text{ej}} \rangle = \frac{2^{-1/2} \pi \rho_0 m G^{1/2} r_0^{5/2} (-4 + 12e^2 + 5(1-e^2)^{3/2})}{(\gamma_* + 1) M^{3/2} a (1-e^2)^{3/2}}. \quad (\text{A4})$$

APPENDIX B: LOCAL DIFFUSION COEFFICIENT

The local diffusion coefficient we evaluate in Eq. 35 is given by (Magorrian & Tremaine 1999; Wang & Merritt 2004):

$$\lim_{R \rightarrow 0} \frac{\langle (\Delta R)^2 \rangle}{2R} = \frac{32\pi^2 r^2 G^2 \langle m_*^2 \rangle \ln \Lambda}{3J_c^2(\epsilon)} (3I_{1/2}(\epsilon) - I_{3/2}(\epsilon) + 2I_0(\epsilon)) \quad (\text{B1})$$

with:

$$I_0(\epsilon) \equiv \int_0^\epsilon f(\epsilon') d\epsilon' \quad (\text{B2})$$

and

$$I_{n/2}(\epsilon) \equiv [2(\psi(r) - \epsilon)]^{-n/2} \int_\epsilon^{\psi(r)} [2(\psi(r) - \epsilon')]^{n/2} f(\epsilon') d\epsilon'. \quad (\text{B3})$$